Inverse Problems and Imaging
Volume 7, No. 1, 2013, 217–242
doi:10.3934/ipi.2013.7.217

RECOVERING BOUNDARY SHAPE AND CONDUCTIVITY IN ELECTRICAL IMPEDANCE TOMOGRAPHY

Ville Kolehmainen

University of Eastern Finland
Department of Applied Physics
P.O.Box 1627, 70211 Kuopio, Finland

Matti Lassas, Petri Ola and Samuli Siltanen

University of Helsinki
Department of Mathematics and Statistics
P.O.Box 68, 00014 University of Helsinki, Finland

(Communicated by Giovanni Alessandrini)

Abstract. Electrical impedance tomography (EIT) aims to reconstruct the electric conductivity inside a physical body from current-to-voltage measurements at the boundary of the body. In practical EIT one often lacks exact knowledge of the domain boundary, and inaccurate modeling of the boundary causes artifacts in the reconstructions. A novel method is presented for recovering the boundary shape and an isotropic conductivity from EIT data. The first step is to determine the minimally anisotropic conductivity in a model domain reproducing the measured EIT data. Second, a Beltrami equation is solved, providing shape-deforming reconstruction. The algorithm is applied to simulated noisy data from a realistic electrode model, demonstrating that approximate recovery of the boundary shape and conductivity is feasible.

1. **Introduction.** In electrical impedance tomography (EIT), the electric conductivity inside a physical body is reconstructed from electric current and voltage measurements at the boundary of the body. EIT has applications in medical imaging, nondestructive testing, geophysical prospection and industrial process monitoring.

Most EIT algorithms rely on the assumption that the shape of the boundary of the body is known exactly. However, that assumption is not always practical, especially in medical applications. For instance, consider monitoring heart and lung function of an unconscious intensive care patient using EIT [13, 24, 25]. The measurement electrodes are attached around the chest of the patient. The shape of a cross-section of the chest could in principle be obtained using another imaging modality such as magnetic resonance imaging, but that option involves transportation and scheduling issues. Further, the shape of the thorax varies due to breathing and changes in the patient position. Therefore, the shape of the boundary would be known only approximately even at the best case. This is problematic as using even slightly incorrect model of the boundary can cause serious errors in the reconstruction [31, 17, 1, 26].

2010 *Mathematics Subject Classification.* Primary: 35R30, 65N21; Secondary: 65J20.

Key words and phrases. Inverse conductivity problem, electrical impedance tomography, minimally anisotropic conductivity, quasiconformal maps, conformal deformation.

This work was supported by the Academy of Finland (projects 141104, 141094, 134868, 119270 and 134868, and Centres of Excellence in Inverse Problems Research 213476 and 250215).

The traditional way in biomedical EIT for reducing partially the effect of inaccurately known body shape has been to use difference imaging, where the objective is to reconstruct the change in the conductivity between two measurement times (or two frequencies) using a first order linear perturbation model [7] [1] The approach is highly approximative since the actual nonlinear forward mapping is approximated by a linear one, but it is computationally fast since the related Jacobian mappings are precomputed (at some guessed conductivity), and iterations are not possible in the first place.

Simultaneous reconstruction of the change in conductivity and electrode movement have been proposed for *difference imaging* in the two-dimensional (2D) case in [45, 16] and in three-dimensions in [33, 38]. These approaches are based on a linearized perturbation model and have been demonstrated only for small temporal changes. While difference imaging can reduce the effect of inaccurately known geometry, some artefacts usually remain [1, 45, 8, 9]. Also, difference imaging is not always satisfactory. For example in high-contrast cases, such as accumulation of well conducting liquid (haematothorax) or poorly conducting air (pneumothorax) in the lungs, the linearization involved may prevent the detection of clinically relevant conditions [23]. Also, the detection of pneumothorax is difficult using difference imaging if the change in the lungs has occurred prior to the measurements [15].

Apart from difference imaging, only a few approaches have been proposed for compensating the effect of inaccurately known boundary shape in EIT. In [40], the Bayesian approximation error approach was applied for the compensation of the inaccurately known boundary shape in (absolute) EIT problem. In the approximation error approach, the modelling error caused by the incorrect boundary model is treated as an additive noise process in the measurement model. A Gaussian approximation for the probability distribution of modelling error noise was estimated using an atlas of body geometries from computerized tomography images, and these statistics were then employed in the image reconstruction process to compensate for the uncertainty in the body shape. In [41], the approach was extended for recovery of a low-rank approximation for the boundary shape based on the approximate joint statistics of the shape and the modelling error.

In this paper, continuing the work reported in [32, 34], we introduce a novel three-step method for the recovery of the conductivity and boundary shape in the absolute EIT problem in the 2D case. See Figure 1 for a demonstration.

In the 2D case, the EIT problem is formulated as follows: Let $\Omega \subset \mathbb{R}^2$ be a bounded and sufficiently smooth domain representing the measurement domain, and let $\gamma = [\gamma^{ij}(x)]_{i,j=1}^2$ be a matrix modeling electrical conductivity in Ω. We assume that γ has components in $L^\infty(\Omega)$ and is strictly positive definite, that is, for some constant $C > 0$ we have

$$C^{-1}\|\xi\|^2 \leq \xi \cdot \gamma(x)\xi \leq C\|\xi\|^2, \quad \text{for } \xi \in \mathbb{R}^2, \text{ a.e. } x \in \Omega. \tag{1}$$

The conductivity γ is called *isotropic* if it has the form of a scalar valued function times identity matrix; otherwise it is called *anisotropic*. In this work we discuss the reconstruction of isotropic conductivities, but intermediate steps in our method involve anisotropic conductivities as well.

[1] As opposed to "difference imaging", the original EIT problem (posed by Calderón) of reconstructing the conductivity function from the current and voltage data is often referred in the biomedical literature as "absolute EIT imaging".

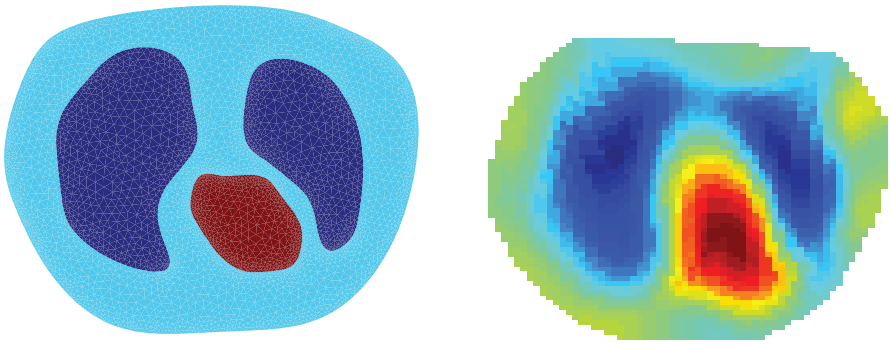

FIGURE 1. Left: original synthetic conductivity. Right: reconstruction, *without knowing the shape of the boundary*, from EIT data simulated with the complete electrode model using 16 electrodes and 42 dB noise level.

Let u denote the electric potential in Ω, where we assume that u belongs to Sobolev space $H^1(\Omega)$. The potential satisfies the conductivity equation

$$\nabla \cdot \gamma \nabla u = 0 \quad \text{in } \Omega. \tag{2}$$

and the Robin boundary condition

$$(z\nu \cdot \gamma \nabla u + u)|_{\partial\Omega} = h.$$

The function z is called *contact impedance* and models voltage drops caused by electrochemical effects at the electrode-skin interface. Measurements are modelled by the Robin-to-Neumann map $R = R_{z,\gamma}$ given by

$$R : h \mapsto \nu \cdot \gamma \nabla u|_{\partial\Omega},$$

mapping the voltage potential distribution at the boundary to the current across the boundary. We assume that the contact impedance function is continuously differentiable and strictly positive: $z \geq c > 0$.

The EIT problem considered in this article is to reconstruct an isotropic conductivity γ inside Ω using values $R_{z,\gamma}g$ for all $g \in H^{-1/2}(\partial\Omega)$. It is shown in [35] that R determines the map z, and hence the knowledge of R is equivalent to the knowledge of the Dirichlet-to-Neumann map much studied in EIT literature.

The EIT problem was formulated mathematically by Calderón [12]. For fundamental results on the unique solvability of the EIT problem in the plane we refer to works of Nachman [39], Brown-Uhlmann [11] and finally Astala-Päivärinta [5] where this problem was settled for general isotropic L^∞-conductivities. Numerical solution of the EIT problem is typically computed, for example, using the regularized least squares framework [13] or the Bayesian inversion framework [27]. For an example on numerical implementation of a direct solution based on the uniqueness proof of Nachman [39], see [44, 24, 30]. A common feature in all those numerical methods is that the boundary of the measurement domain Ω is assumed to be known.

We consider recovering an unknown isotropic conductivity γ in Ω and an approximation to the unknown shape of $\partial\Omega$ from discrete current-to voltage measurements performed using N electrodes on the boundary $\partial\Omega$. In practice, the data is a finite matrix that approximates the Robin-to-Neumann map R.

The starting point is to choose a *model domain*, the best available approximation Ω_m to the actual domain Ω. For example, Ω_m can be a disc having roughly the same area than Ω. We build a computational model for discrete Robin-to-Neumann data from a given (possibly anisotropic) conductivity in Ω_m measured using J electrodes on $\partial\Omega_m$. Our reconstruction algorithm consists of the following steps:

1. **Recovering minimally anisotropic conductivity.** Compute $\gamma_e(x)$, the least anisotropic of all conductivities in the model domain Ω_m producing the same data matrix than was measured on $\partial\Omega$. Under our assumptions there is a unique γ_e. Furthermore, the function
$$\eta(x) := \det(\gamma_e(x))^{1/2}$$
represents a geometrically distorted image inside Ω_m of the original isotropic conductivity. See [32, 35] for the numerical implementation of this step.
2. **Isotropization.** Determine numerically isothermal coordinates $x \mapsto F_i(x)$ corresponding to γ_e. This step gives approximate recovery of the domain deformation and boundary shape. The details of the numerical implementation of Step 2, the main computational novelty of this paper, are in Section 4.2.
3. **Shape-deforming reconstruction.** Use the isothermal coordinates to reconstruct the original isotropic conductivity approximately as
$$\eta(\mathrm{Re}(F_i(x)), \mathrm{Im}(F_i(x))).$$

This paper is organized as follows. In Section 2 we give the details of the theory of shape-deforming reconstruction. Section 3 is devoted to explaining the simulation of discrete and noisy EIT measurements. In Section 4 we explain numerical implementation of the theoretical ideas described in Section 2. Numerical results are reported in Section 5, and finally, reasons behind the good performance of our method are discussed in Section 6.

2. Theory of shape-deforming reconstruction.

2.1. Recovering minimally anisotropic conductivity.

Quasiconformal maps are the basic tools of our method. Conformal maps in two-dimensional space are deformations that preserve angles and map discs to discs. Quasiconformal maps are more general as they may distort angles to some extent, but not arbitrarily much.

Let us record the definition and basic properties of quasiconformal maps. Let $\Omega, \tilde{\Omega} \subset \mathbb{C}$ be open sets. An orientation-preserving homeomorphism $F : \Omega \to \tilde{\Omega}$ is called K-quasiconformal if
$$D(x) \le K \quad \text{for a.e. } x \in \Omega, \text{ where } D(x) = \frac{|\partial F(x)| + |\overline{\partial} F(x)|}{|\partial F(x)| - |\overline{\partial} F(x)|} \ge 1.$$
Here, $\partial = \frac{1}{2}(\partial_{x_1} - i\partial_{x_2})$, $\overline{\partial} = \frac{1}{2}(\partial_{x_1} + i\partial_{x_2})$, and $x = x_1 + ix_2$. The constant K controls the extent to which angles can be distorted under F.

There is also a geometric definition of quasiconformal maps. Conformal maps take infinitesimal discs at x to infinitesimal discs at $f(x)$, and the radii get dilated by $|f'(x)|$. More generally, a homeomorphism f is quasiconformal on a domain Ω if infinitesimal discs at any $x \in \Omega$ get mapped to infinitesimal ellipses at $f(x)$. The ratio of the larger semiaxis to smaller semiaxis is the dilation $D(x)$ of f at x, and taking the supremum over $x \in \Omega$ yields the so-called maximal dilation. This dilation of infinitesimal discs is in fact the reason why isotropic conductivities change to anisotropic ones in push-forwards with quasiconformal maps.

The inaccurately known boundary can be considered as the boundary of the deformed model domain. Such a deformation corresponds to a sufficiently smooth diffeomorphism F that maps the original measurement domain Ω to another domain $\widetilde{\Omega}$. Denote $f = F|_{\partial\Omega}$. Then, if u solves (2) with a Robin boundary value h, $\widetilde{u} = u \circ F^{-1}$ and $\tilde{h}(x) = h(f^{-1}(x))$, it can be shown that $\widetilde{u}$ solves the conductivity equation

$$\begin{aligned} \nabla\cdot\tilde{\gamma}\nabla\tilde{u} &= 0, \quad \text{in } \tilde{\Omega}, \\ \tilde{z}\nu\cdot\tilde{\gamma}\nabla\tilde{u} + \tilde{u}|_{\partial\tilde{\Omega}} &= \tilde{h}, \end{aligned} \tag{3}$$

where $\tilde{z}(x) = z(f^{-1}(x))\|\tau\cdot\nabla(f^{-1})(x)\|$ with τ the unit tangent vector of $\partial\tilde{\Omega}$, and $\tilde{\gamma}$ is the conductivity

$$\tilde{\gamma}(x) := F_*\gamma(x) = \left.\frac{F'(y)\,\gamma(y)\,(F'(y))^{\mathrm{T}}}{|\det F'(y)|}\right|_{y=F^{-1}(x)}, \tag{4}$$

where $F' = DF$ is the Jacobian matrix of map F, and $F_*\gamma$ is called the push-forward of γ by F. The boundary measurements transform according to the formula

$$(\tilde{R}h)(x) = (R(h\circ f))(y)|_{y=F^{-1}(x)}\,. \tag{5}$$

where $\tilde{R}$ corresponds to conductivity $\tilde{\gamma}$ and contact impedance $\tilde{z}$ in domain $\tilde{\Omega}$. Note that formula (4) implies that even if γ is isotropic, the transformed conductivity $\widetilde{\gamma}$ will in general be anisotropic. It is well known (see [28, 48, 39] and also [4, 37, 36]) that the Dirichlet-to-Neumann map, and hence also the Robin-to-Neumann map, does not determine uniquely an anisotropic conductivity. When the anisotropy is very strong it is even possible to construct counterexamples for unique solvability of the inverse conductivity problem up to change of coordinates [21, 22, 29]. These examples are closely related to the so-called invisibility cloaking see e.g. [18, 19, 20].

Our set-up is motivated by the fact that the quadratic form corresponding to the pushed-forward Robin-to-Neumann map R_m,

$$R_m[g,g] = \int_{\partial\Omega_m} g\,R_m g\,dS = \int_{\partial\Omega} (g\circ f_m)\,R_\gamma(g\circ f_m)\,dS, \qquad h\in H^{-1/2}(\partial\Omega_m)$$

represents the power needed to maintain $g\circ f_m$ on the original boundary $\partial\Omega$. Knowing R_m is equivalent to knowing the corresponding quadratic form.

Let us first consider a conventional approach to solve the EIT inverse problem by minimizing the regularized least squares cost functional

$$\|R_m - R_{z,\gamma}\|^2_{L(H^{-1/2}(\partial\Omega_m),H^{-1/2}(\partial\Omega_m))} + \alpha\|\gamma\|^2_X \tag{6}$$

over isotropic conductivities γ in the model domain Ω_m. Here $\|\cdot\|_X$ is some regularization norm, $\alpha > 0$ is a regularization parameter and $L(X,Y)$ denotes the space of linear bounded operator from X to Y. Since R_m usually does not correspond to any isotropic conductivity because of the deformation done when going from the original domain Ω to Ω_m, we obtain an erroneous reconstruction γ when solving the minimization problem (6). A systematic error in the domain model causes a systematic error to the reconstruction. In particular, local changes of the conductivity often give rise to non-localized changes in the reconstructions due to the above modelling error. Thus the spatial resolution of details of reconstructions are often weak. This is clearly seen in practical measurements, see e.g. [17, 31].

To overcome the above difficulties and to reconstruct a conductivity up to a conformal deformation close to the original conductivity, we first find in Ω_m an anisotropic conductivity that is as close as possible to isotropic conductivities, and

then use the existence of isothermal coordinates to find a deformation that makes the conductivity isotropic. In particular, in such a construction the obtained deformation is small if the errors in the modeling of the domain are small. To explain how this is done, we first recall (with slightly different notations) the quantitative definition of anisotropy used in [32]:

Definition 2.1. Let $[\gamma^{jk}(x)]_{j,k=1}^2$ be a matrix-valued conductivity with elements in $L^\infty(\Omega)$ and let $\lambda_1(x)$ and $\lambda_2(x)$, $\lambda_1(x) \geq \lambda_2(x)$ be the eigenvalues of $\gamma^{jk}(x)$. We define the maximal anisotropy of a conductivity to be $A(\gamma)$ given by

$$A(\gamma) = \sup_{x\in\Omega} A(\gamma, x), \quad \text{where} \quad A(\gamma,x) = \frac{\sqrt{\lambda(x)}-1}{\sqrt{\lambda(x)}+1}, \quad \lambda(x) = \frac{\lambda_1(x)}{\lambda_2(x)}.$$

The function $A(\gamma, x)$ is the anisotropy of γ at x.

Note that if F is K-quasiconformal and γ is an isotropic conductivity, then

$$A(F_*\gamma) = \frac{K-1}{K+1}. \tag{7}$$

Using a classical result of Strebel (see [47], [10]) on the existence of the extremal quasiconformal map, it was observed in [32] that among all anisotropic conductivities in the model domain Ω_m with a given Dirichlet-to-Neumann map, or equivalently R_m, there is a unique conductivity γ_e that has the minimal anisotropy $A(\gamma_e)$ and that this conductivity γ_e is of the form $\gamma_e = \hat{\gamma}_{\lambda,\theta,\eta}$,

$$\hat{\gamma}_{\lambda,\theta,\eta}(x) = \eta(x)\mathcal{R}_{\theta(x)} \begin{pmatrix} \lambda^{1/2} & 0 \\ 0 & \lambda^{-1/2} \end{pmatrix} \mathcal{R}_{\theta(x)}^{-1}, \tag{8}$$

where $\lambda \geq 1$ is a constant, $\eta(x) \in \mathbb{R}_+$ is a real-valued function with the property

$$\eta(x) = \det(\gamma_e(x))^{1/2}$$

and $\mathcal{R}_{\theta(x)}$ is a rotation matrix corresponding to angle $\theta(x)$,

$$\mathcal{R}_\theta = \begin{pmatrix} \cos\theta & \sin\theta \\ -\sin\theta & \cos\theta \end{pmatrix}. \tag{9}$$

Note that for the conductivities $\hat{\gamma} = \hat{\gamma}_{\lambda,\theta,\eta}$ the anisotropy $A(\hat{\gamma}, x)$ is constant in x,

$$A(\hat{\gamma}, x) = \frac{\lambda^{1/2}-1}{\lambda^{1/2}+1}. \tag{10}$$

This is why we call such conductivities $\hat{\gamma}$ *uniformly anisotropic conductivities*. Moreover, there is a unique map $F_e : \Omega \to \Omega_m$ such that $F_e|_{\partial\Omega} = f_m$ and $\gamma_e = (F_e)_*\gamma$, and the conductivity γ_e can be used to compute in Ω_m a deformed image of the original conductivity γ defined in Ω, namely, we have

$$\det(\gamma_e(x))^{1/2} = \gamma(y), \quad y = F_e^{-1}(x), \ x \in \Omega_m, \tag{11}$$

see [32]. Note that R_m determines γ_e, but not the original domain Ω or the map $F_e : \Omega \to \Omega_m$, the extremal quasiconformal map with boundary value f_m.

Analogously to [32], with given R_m the conductivity γ_e can be found as the unique solution of the minimization problem

$$\begin{aligned} &\min_{(\lambda,\theta,\eta)\in S} \lambda, \\ &S = \{(\lambda,\theta,\eta) \in [1,\infty) \times L^\infty(\Omega_m) \times L^\infty(\Omega_m) |\ R_{\hat{\gamma}(\lambda,\theta,\eta)} = R_m\}. \end{aligned} \tag{12}$$

Note that in implementation of the algorithm for noisy measurement data one can approximate the problem (12) with the regularized minimization problem

$$\min_{(\lambda,\theta,\eta)} \|R_{\tilde{\gamma}(\lambda,\theta,\eta)} - R_m\|^2_{L(H^{-1/2}(\partial\Omega_m),H^{-1/2}(\partial\Omega_m))} + \varepsilon_1 f(\lambda) + \varepsilon_2\|\theta\|^2_{H^1(\Omega_m)} + \varepsilon_2\|\eta\|^2_{H^1(\Omega_m)}, \tag{13}$$

where $f : [1,\infty) \to \mathbb{R}_+$ is a convex function that has its minimum at $\lambda = 1$ and $\lim_{t\to\infty} f(t) = \infty$ and $\varepsilon_1, \varepsilon_2, \varepsilon_3 > 0$ are regularization parameters.

2.2. **Isotropization.** Below we use tools of complex analysis and identify $\mathbb{C}$ and $\mathbb{R}^2$. We extend the minimization algorithm (12) and its approximation (13) by transforming the reconstructed conductivity γ_e to an isotropic conductivity. This is done by extending γ_e by an isotropic unit conductivity to whole $\mathbb{C}$, and defining $F_i : \mathbb{C} \to \mathbb{C}$ be the unique solution of the problem

$$\overline{\partial} F_i(x) = \mu(x)\partial F_i(x), \quad x \in \mathbb{C}, \tag{14}$$

$$F_i(x) = x + h(x), \tag{15}$$

$$h(x) \to 0 \text{ as } |x| \to \infty. \tag{16}$$

Here

$$\mu(x) = \frac{\gamma_{e,11} - \gamma_{e,22} + 2i\gamma_{e,12}}{\gamma_{e,11} + \gamma_{e,22} + 2\sqrt{\det \gamma_e}}, \quad \gamma_e = \left[\gamma_{e,jk}(x)\right]_{j,k=1}^2. \tag{17}$$

Equation (14) has a unique solution by [2] as $|\mu(x)| \le c_0 < 1$ and $\mu(x)$ vanishes outside Ω_m. Note that the map $x \mapsto F_i(x)$ can be considered as the isothermal coordinates in which γ_e can be represented as an isotropic conductivity, and that the Beltrami coefficient is related to the anisotropy defined in (10) via the following formula: $|\mu(x)| = A(\hat{\gamma}, x)$ for $x \in \Omega_m$. We say that the conductivity γ_e is isotropized by defining

$$\gamma_i = (F_i)_*\gamma_e$$

according to the formula (4). The conductivity γ_i is isotropic, and actually

$$\gamma_i(x) = (\det \gamma_e)^{1/2} \circ F_i^{-1}(x) = \gamma \circ (F_i \circ F_e)^{-1}(x), \quad x \in \Omega_i = F_i(\Omega_m). \tag{18}$$

In the following, we denote $G = F_i \circ F_e : \Omega \to F_i(\Omega_m)$. The above procedure and [34] give us the following result:

Proposition 1. *Let Ω be a bounded, simply connected $C^{1,\alpha}$-domain with $\alpha > 0$. Assume that $\gamma \in L^\infty(\Omega)$ is an isotropic conductivity and R_γ its Robin-to-Neumann map. Let Ω_m be a model of the domain satisfying the same regularity assumptions as Ω, and $f_m : \partial\Omega \to \partial\Omega_m$ be a $C^{1,\alpha}$-smooth orientation preserving diffeomorphism.*

Assume that we are given $\partial\Omega_m$ and $R_m = (f_m)_*R_\gamma$. Let γ_e be solution of the minimization problem (12), F_i be the solution of the equations (14)-(17), and $\gamma_i = (F_i)_*\gamma_e$. Then

$$\gamma_i(x) = \gamma(G^{-1}(x)), \quad x \in \Omega_i = F_i(\Omega_m) \tag{19}$$

where $G : \Omega \to \Omega_i$ is a conformal map.

2.3. **Shape-deforming reconstruction.** Thus the obtained conductivity γ_i can be considered as a conformally deformed image of the conductivity γ. As the map F_e corresponds to the minimally anisotropic conductivity and the maps F_i and G are related to the isotropization of the minimally anisotropic conductivity, the deformation G obtained above is small if $F_e : \Omega \mapsto \Omega_m$ is close to identity.

We will discuss the properties of this step further in Section 6.

3. Simulation of EIT data.

3.1. **Electrode model.** In practical EIT experiments, the data consists of a finite number of voltage and current measurements that are taken using a set of electrodes attached at the boundary $\partial\Omega$. To model these measurements accurately, we employ the so-called complete electrode model [46, 14], which is a certain finite-dimensional approximation of the Robin-to-Neumann map.

Let $e_j \subset \partial\Omega$, $j = 1, \ldots, J$ be disjoint open paths modelling the electrodes that are used for the measurements. In the electrode model, the boundary conditions for the conductivity equation (2) are:

$$z_j \nu \cdot \gamma \nabla u + u|_{e_j} = U_j, \tag{20}$$

$$\nu \cdot \gamma \nabla u|_{\partial\Omega \setminus \cup_{j=1}^{J} e_j} = 0, \tag{21}$$

where U_j are constants representing electric potentials on electrode e_j. This models the case where electrodes e_j having potentials U_j are attached to the boundary, z_j is the contact impedance between electrode e_j and the body surface, and the normal current outside the electrodes vanish (the gaps are insulated).

The existence and uniqueness of the solution (u, U), where $u \in H^1(\Omega)$ and $U = (U_1, \ldots, U_J)^{\mathrm{T}} \in \mathbb{R}^J$ is quaranteed by the charge conservation

$$\sum_{\ell=1}^{J} I_\ell = 0. \tag{22}$$

and by fixing the ground level of the potentials

$$\sum_{\ell=1}^{J} U_\ell = 0, \tag{23}$$

for details see [46].

The measurements in this model are the currents observed on the electrodes, given by

$$I_j = \frac{1}{|e_j|} \int_{e_j} \nu \cdot \gamma \nabla v(x)\, ds(x), \quad j = 1, \ldots, J.$$

Thus the electrode measurements are given by map

$$E : \mathbb{R}^J \to \mathbb{R}^J, \quad E(U_1, \ldots, U_J) = (I_1, \ldots, I_J).$$

We say that E is the electrode measurement matrix for $(\partial\Omega, \gamma, e_1, \ldots, e_J, z_1, \ldots, z_J)$.

The conditions for the applicability of the algorithm (12) in case of the electrode model (20)-(21) are given in Proposition 4.1 in [32]. In summary, when Ω_m is our model of Ω and the map $f_m : \partial\Omega \to \partial\Omega_m$ is the model map for the boundary, the map f_m has to be length preserving on the electrodes. From the practical point of view, this means the very natural assumption that in electrode measurements the size of the electrodes has to be known correctly.

Another discussion of boundary perturbations is given in [8], studying the effect of small boundary perturbations in linearized difference imaging induced by various vector fields.

3.2. **Discretization and notation.** The finite dimensional approximation and numerical solution of the model (2),(20)-(23) is based on the finite element method (FEM). Detailed description on the variational form and FEM implementation of the model with anisotropic (matrix valued) conductivities is given in [35]. Here we give only the notation for the discretized problem.

In the discretized model, we represent the functions $\eta(x)$ and $\theta(x)$ in equation (8) as images on a finite dimensional pixel grid. That is, we write piecewise constant approximations

$$\eta(x) = \sum_{k=1}^{M} \eta_k \chi_k(x), \quad \theta(x) = \sum_{k=1}^{M} \theta_k \chi_k(x) \tag{24}$$

where χ_k is the characteristic function of the k^{th} pixel in the pixel grid and η_k, θ_k are the pixel values of the parameters. With the representation (24), the parameters η and θ are identified with the coefficient vectors

$$\eta = (\eta_1, \eta_2, \ldots, \eta_M)^{\mathrm{T}} \in \mathbb{R}^M, \quad \theta = (\theta_1, \theta_2, \ldots, \theta_M)^{\mathrm{T}} \in \mathbb{R}^M$$

and λ is a scalar parameter.

In practical EIT devices, the measurements are made so that known currents are injected into the domain Ω through some of the electrodes at $\partial\Omega$, and the corresponding voltages needed to maintain these currents are measured on some of the electrodes. Often, voltages are measured only on those electrodes that are not used to inject current. Thus, measurements made give only partial information on the matrix E. To take this in to account, we introduce the following notation for the discretized problem. We assume that the EIT experiment consists of a set of K partial voltage measurements, $V^{(j)}$, $j = 1, \ldots, K$. For each measurement, consider a current pattern $I^{(j)} \in \mathbb{R}^J$, $j = 1, \ldots, K$ such that the vector $I^{(j)}$ fullfills the charge conservation law (22). Typically, the corresponding measurements are the voltages (potential differences) between pairs of neighboring electrodes. Let us assume that the measurement vector $V^{(j)}$ corresponding to the current pattern $I^{(j)}$ consist of L voltage measurements, i.e., we have $V^{(j)} \in \mathbb{R}^L$. To take the presence of measurement noise into account, we model the measurement vector $V^{(j)}$ by the additive noise model:

$$V^{(j)} = P_j E^{-1} I^{(j)} + \epsilon^{(j)},$$

where E is the electrode measurement matrix obtained from the FEM discretization (for details see [35]), random vector $\epsilon^{(j)}$ models the measurement errors and $P_j : \mathbb{R}^J \to \mathbb{R}^L$ is a measurement operator that maps the electrode potentials to the voltages.

In the computations, the voltage measurement vectors $V^{(1)}, V^{(2)}, \ldots, V^{(K)}$ are concatenated into a single measurement vector

$$V = (V^{(1)}, V^{(2)}, \ldots, V^{(K)})^{\mathrm{T}} \in \mathbb{R}^N, \quad N = KL.$$

For the finite element based discretization of the forward problem $U : \mathbb{R}^{2M+1} \mapsto \mathbb{R}^N$, we use respectively the notation

$$U(\eta, \theta, \lambda) = (U^{(1)}(\eta, \theta, \lambda), U^{(2)}(\eta, \theta, \lambda), \ldots, U^{(K)}(\eta, \theta, \lambda))^{\mathrm{T}} \in \mathbb{R}^N.$$

Here,

$$U^{(j)}(\eta,\theta,\lambda) = P_j E^{-1}(\eta,\theta,\lambda) I^{(j)} \in \mathbb{R}^L$$

corresponds to partial voltage measurement with current pattern $I^{(j)}$ and conductivity $\hat{\gamma}_{\eta,\theta,\lambda}$.

3.3. **Simulation examples and parameters.** We demostrate the reconstruction method using simulated measurement data from four test cases:

- **(Case 1):** The measurement domain Ω is an ellipse with main axes 17cm and 12cm in the x_1 and x_2 directions, respectively.
- **(Case 2):** The measurement domain Ω is a truncated ellipse with main axes 12cm and 17cm in in the x_1 and x_2 directions, respectively. The truncation surfaces are defined by setting $x_1 = \min(x_1, 10)$ and $x_2 = \min(x_2, 15)$.
- **(Case 3):** The measurement domain Ω is bounded by a smooth curve.
- **(Case 4):** The measurement domain Ω is segmented from a computerized tomography image of the human chest.

The boundary of the measurement domain $\partial\Omega$ for each of the test cases is shown in Figure 2 with solid line.

In all four cases, we used a circle with radius of 14 cm as the model domain Ω_m. The model domain is illustrated with gray patch in Figure 2. In the computations, the model domain Ω_m was discretized to a FEM mesh with $N_e = 4968$ triangular elements and $N_n = 2677$ node points. For the representation of the conductivity, Ω_m was divided to $M = 1021$ square pixels with pixel size $8 \times 8\text{mm}^2$.

We simulated an EIT system with $J = 16$ electrodes. The electrodes were located at approximately equally spaced positions at the boundary $\partial\Omega$ of the target domain Ω. The EIT measurements were simulated using the traditional adjacent pair drive data acquisition method, where currents $+1$ and -1 are injected through two neighboring electrodes, say electrodes e_n and e_{n+1}, and current through other electrodes is zero. The voltages are measured between all $J-3$ pairs of electrodes with zero current. Each partial measurement consists of $L = J-3$ voltage measurements and we have $V^{(j)} \in \mathbb{R}^{J-3}$. This process is then repeated for all the J pairs of adjacent electrodes, leading to total of $N = J(J-3)$ voltage measurements. Thus, with the $J = 16$ electrode system we have measurement vector $V \in \mathbb{R}^{208}$.

In all test cases we constructed isotropic target conductivity in the measurement domain Ω. The simulated EIT measurements were computed using FEM. To avoid inverse crime, the simulated measurement and the reconstructions were computed using different FEM meshes. The numbers of node points N_n and triangle elements N_e in the FEM meshes used in the data simulation are listed in Table 1. We added Gaussian random noise with signal-to-noise ratio 42dB to the data. We chose contact impedances $z_\ell = 1$ and assumed them known in the reconstruction.

4. Shape-deforming reconstruction algorithm.

4.1. **Recovering minimally anisotropic conductivity.** We need to solve the constrained minimization problem (13). As the first step, we note that as uniformly anisotropic conductivities of the form (8) have the property $\hat{\gamma}_{\lambda,\eta,\theta} = \hat{\gamma}_{\lambda',\eta,\theta'}$, where $\lambda' = 1/\lambda$ and $\theta'(x) = \theta(x) + \pi/2$, we can reparameterize (13) such that λ gets values $\lambda > 0$, meaning that we get a more simple form that has positivity constraints only. Thus, using the re-parameterization we write the discretized version of (13) as

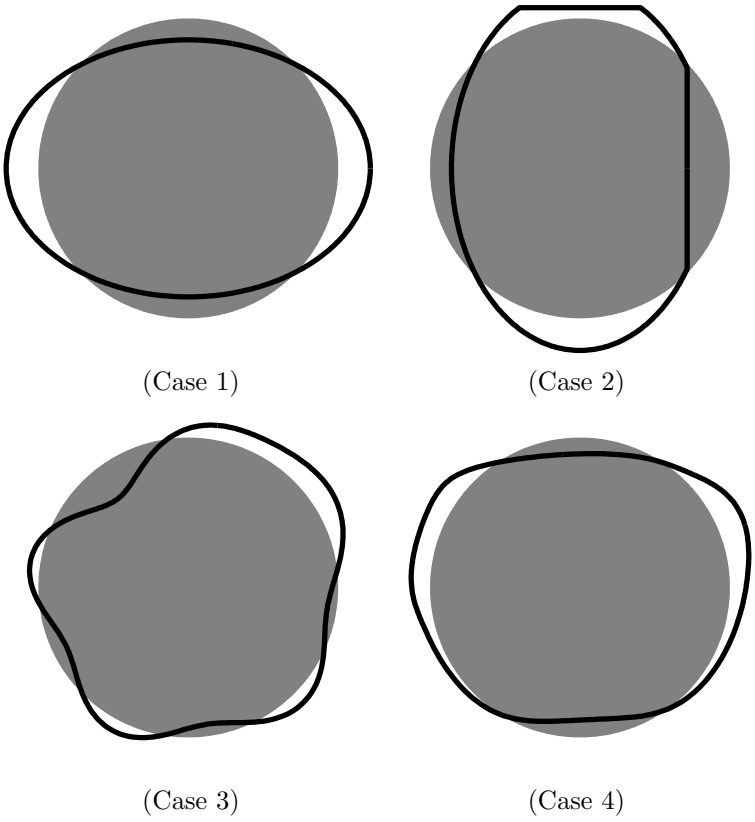

Figure 2. Measurement domain Ω in the Cases 1-4 ($\partial\Omega$ is shown with solid line). The model domain Ω_m in all cases is a circle with radius 14 cm (Ω_m is shown as gray patch).

finding the minimizer of

$$F(\eta,\theta,\lambda) = \|V - U(\eta,\theta,\lambda)\|^2 + W_\eta(\eta) + W_\theta(\theta) + W_\lambda(\lambda), \quad \eta > 0, \lambda > 0, \tag{25}$$

where parameters η, θ, λ define a uniformly anisotropic conductivity of the form (8) in Ω_m and the regularizing penalty functionals are of the form

$$W_\eta(\eta) = \alpha_0 \sum_{k=1}^{M} \eta_k^2 + \alpha_1 \sum_{k=1}^{M} \sum_{j\in\mathcal{N}_k} |\eta_k - \eta_j|^2, \tag{26}$$

$$W_\theta(\theta) = \beta_0 \sum_{k=1}^{M} \theta_k^2 + \beta_1 \sum_{k=1}^{M} \sum_{j\in\mathcal{N}_k} |e^{i\theta_k} - e^{i\theta_j}|^2, \tag{27}$$

$$W_\lambda(\lambda) = \beta_2(\lambda - 1)^2, \tag{28}$$

α_0,α_1,β_0,β_1,β_2 are non-negative, scalar valued regularization parameteres and $\mathcal{N}_k$ denotes the 4-point nearest neighborhood system for pixel k in the pixel grid. In principle, one could attempt minimization of (25) by constrained non-linear optimization methods, which can be computationally involved [42]. To tranform the

optimization problem into computationally less demanding form, we utilize a second transformation of the variables as

$$(\xi, \theta, \zeta), \quad \xi = \log(\eta) \in \mathbb{R}^M, \theta \in \mathbb{R}^M, \quad \zeta = \log(\lambda) \in \mathbb{R}, \tag{29}$$

transforming the constrained optimization problem (25) into an *unconstrained* one

$$F(\xi, \theta, \zeta) = \|V - U(\exp(\xi), \theta, \exp(\zeta))\|^2 + W_\eta(\exp(\xi)) + W_\theta(\theta) + W_\lambda(\exp(\zeta)), \tag{30}$$

that can be solved by gradient based optimization techniques for unconstrained optimization, for examples of the methods see [42]. In this study, the minimization of (30) is carried out with the Gauss-Newton optimization method equipped with an explicit line search algorithm, for details see [42].

4.2. **Isotropization.** Given the estimates

$$\eta = \exp(\xi), \quad \theta, \quad \lambda = \exp(\zeta)$$

that define the estimated uniformly anisotropic conductivity in the model domain Ω_m, the second step of our algorithm consists of the isotropization of the anisotropic conductivity. For this step, we need to find the mapping $F_i(x)$ by solving the equations (14)-(17) numerically as follows.

Define the solid Cauchy transform by

$$Pf(x) = -\frac{1}{\pi} \int_{\mathbb{C}} \frac{f(\lambda)}{\lambda - x} d\lambda, \tag{31}$$

and Beurling transform by $Sf = \partial Pf$. Here $x = x_1 + ix_2$ and $\lambda = \lambda_1 + i\lambda_2$ and $d\lambda = d\lambda_1 d\lambda_2$ denotes the usual Lebesgue measure in the plane. Note that P is the inverse operator of $\overline{\partial}$ and that S transforms $\overline{\partial}$ derivatives into ∂ derivatives: $S(\overline{\partial} f) = \partial f$. The Beurling transform can be written as a principal value integral

$$Sf(x) = -\frac{1}{\pi} \int_{\mathbb{C}} \frac{f(w)}{(w - x)^2} dw. \tag{32}$$

Substituting (15) to (14) gives $\overline{\partial} h(x) = \mu(x) + \mu(x)\partial h(x) = \mu(x) + \mu(x) S(\overline{\partial} h)(x)$, which can be written in the form

$$h(x) = P[I - \mu S]^{-1} \mu(x). \tag{33}$$

The inverse operator in (33) is well-defined as it can be expressed as a convergent Neumann series using the fact that $|\mu(x)| < 1$.

We introduce a periodic version of equation (33) as follows. Let $R > 0$ be so large that $\mathrm{supp}(\mu) \subset \Omega_m \subset B(0, R)$. Take $\epsilon > 0$ and set $s = 2R + 3\epsilon$ and define a square $Q := [-s, s)^2$. Choose a smooth cutoff function

$$\eta \in C_0^\infty(\mathbb{R}^2), \qquad \eta(x) = \begin{cases} 1 & \text{for } |x| < 2R + \epsilon, \\ 0 & \text{for } |x| > 2R + 2\epsilon. \end{cases} \tag{34}$$

Define a $2s$-periodic approximate Green's function $\tilde{g}$ by setting it to $\eta(x)/(\pi x)$ inside Q and extending periodically:

$$\tilde{g}(x + j2s + i\ell 2s) = \frac{\eta(x)}{\pi x} \qquad \text{for } x \in Q \setminus 0, \quad j, \ell \in \mathbb{Z}. \tag{35}$$

Formula (31) can be viewed as convolution on the plane with the non-periodic Green's function $1/(\pi x)$. Define a periodic approximate Cauchy transform by

$$\tilde{P} f(x) = (\tilde{g} \tilde{*} f)(x) = \int_Q \tilde{g}(x - w) f(w) dw, \tag{36}$$

where $\tilde{*}$ denotes convolution on the torus. Further, an approximate Beurling transform is defined in the periodic context by writing

$$\tilde{\beta}(x + j2s + i\ell 2s) = \frac{\eta(x)}{\pi x^2} \qquad \text{for } x \in Q \setminus 0, \quad j, \ell \in \mathbb{Z},$$

and setting, analogously to (32), $\tilde{S}f(x) := (\tilde{\beta} \,\tilde{*}\, f)(x) = \int_Q \tilde{\beta}(x-w)f(w)dw$. Now the desired periodic version of equation (33) takes the form

$$\tilde{h}(x) = \tilde{P}[I - \tilde{\mu}\tilde{S}]^{-1}\tilde{\mu}(x), \tag{37}$$

where $\tilde{\mu}$ is the trivial periodic extension of μ.

The practical benefit of considering equation (37) instead of (33) is the finite computational domain of (37), allowing straightforward numerical evaluation. The solution of (37) can then be used to compute the solution of (33) as follows:

Let φ be a function with $\operatorname{supp}(\varphi) \subset B(0,R)$, and denote by $\tilde{\varphi}$ the periodic extension of φ. Since the functions $(\pi\zeta)^{-1}$ and $\tilde{g}(\zeta)$ coincide for $|\zeta| = |x-w| < 2R + \epsilon$, the following identity holds for $|x| < R + \epsilon$:

$$(P\varphi)(x) = \frac{1}{\pi}\int_{\mathbb{D}} \frac{\varphi(w)}{x-w}dw = \int_Q \tilde{g}(x-w)\tilde{\varphi}(w)dw = (\tilde{P}\tilde{\varphi})(x). \tag{38}$$

Now we can write (33) and (37) using Neumann series as follows:

$$h = P\Big(\mu + \mu S(\mu) + \mu S(\mu S(\mu)) + \mu S(\mu S(\mu S(\mu))) + \cdots\Big), \tag{39}$$

$$\tilde{h} = \tilde{P}\Big(\tilde{\mu} + \tilde{\mu}\tilde{S}(\tilde{\mu}) + \tilde{\mu}\tilde{S}(\tilde{\mu}\tilde{S}(\tilde{\mu})) + \tilde{\mu}\tilde{S}(\tilde{\mu}\tilde{S}(\tilde{\mu}\tilde{S}(\tilde{\mu}))) + \cdots\Big). \tag{40}$$

The series in (39) and (40) converge in $L^2(\Omega)$ because $\|S\|_{\mathcal{L}(L^2(\mathbb{R}^2))} = 1$ and $\|\mu\|_{L^\infty(\mathbb{R}^2)} < 1$. Since μ is supported in $B(0,R)$, a combination of (38) and (39) and (40) yields

$$\tilde{h}(x) = h(x) \qquad \text{for } |x| < R. \tag{41}$$

Thus we may evaluate the function $h(x_0)$ at any point $x_0 \in \mathbb{C}$ approximately:

1. Evaluate the function $\tilde{h}(x)$ approximately for a fine grid of points $x \in B(0,R)$ by truncating the infinite sum in formula (40). Numerical implementation of operators $\tilde{P}$ and $\tilde{S}$ is discussed in detail below.
2. If $x_0 \in B(0,R)$, then by (41) we have $h(x_0) = \tilde{h}(x_0)$ and can interpolate.
3. If $x_0 \notin B(0,R)$, then by (41) we can write $h(x_0) = P((\overline{\partial}\,\tilde{h})|_{B(0,R)})(x_0)$. The $\overline{\partial}$ derivative can be approximated by finite differences, and the non-periodic Cauchy transform P is easy to implement using numerical quadrature in (31).

It remains to explain the implementation of the operators $\tilde{P}$ and $\tilde{S}$. Choose a positive integer m, denote $M = 2^m$, and set $h = 2s/M$. Define a grid $\mathcal{G}_m \subset Q$ by

$$\begin{aligned} \mathcal{G}_m &= \{jh \,|\, j \in \mathbb{Z}^2_m\}, \\ \mathbb{Z}^2_m &= \{j = (j_1, j_2) \in \mathbb{Z}^2 \,|\, -2^{m-1} \le j_\ell < 2^{m-1},\ \ell = 1,2\}. \end{aligned} \tag{42}$$

Note that the number of points in $\mathcal{G}_m$ is M^2. Define the grid approximation $\varphi_h : \mathbb{Z}^2_m \to \mathbb{C}$ of a function $\varphi : Q \to \mathbb{C}$ by $\varphi_h(j) = \varphi(jh)$. Set

$$\tilde{g}_h(j) = \begin{cases} \tilde{g}(jh), & \text{for } j \in \mathbb{Z}^2_m \setminus 0, \\ 0, & \text{for } j = 0; \end{cases} \tag{43}$$

note that here the point $jh \in \mathbb{R}^2$ is interpreted as the complex number $hj_1 + ihj_2$. Now $\tilde{g}_h$ is simply a $M \times M$ matrix with complex entries. Given a periodic function φ, the transform $\tilde{P}\varphi$ is approximately given by

$$(\tilde{P}\varphi_h)_h = h^2\, \mathcal{F}^{-1}\big(\mathcal{F}(\tilde{g}_h) \cdot \mathcal{F}(\varphi_h)\big), \tag{44}$$

where $\mathcal{F}$ stands for discrete Fourier transform and $\cdot$ denotes element-wise matrix multiplication. This approach is based on the fact that convolution $\tilde{*}$ on the torus becomes multiplication under the discrete Fourier Transform. The discrete Beurling transform is given by

$$(\tilde{S}\varphi_h)_h = h^2\, \mathcal{F}^{-1}\big(\mathcal{F}(\tilde{\beta}_h) \cdot \mathcal{F}(\varphi_h)\big), \tag{45}$$

where $\tilde{\beta}_h$ is the complex-valued $M \times M$ matrix

$$\tilde{\beta}_h(j) = \begin{cases} \tilde{\beta}(jh), & \text{for } j \in \mathbb{Z}^2_m \setminus 0, \\ 0, & \text{for } j = 0. \end{cases} \tag{46}$$

4.3. **Shape-deforming reconstruction.** Once the numerical approximation of the mapping $F_i(x) = x + h(x)$ has been found, we compute $\eta(\mathrm{Re}(F_i(x)), \mathrm{Im}(F_i(x)))$ as the reconstruction of the original isotropic conductivity. The only practical computation required by this step is interpolation of $\eta(\mathrm{Re}(F_i(x)), \mathrm{Im}(F_i(x)))$ from the irregular grid, which is given by numerical solution of $F_i(x)$.

Table 1. Discretization details for the measurement domain Ω in the test cases. N_e is the number of triangle elements and N_n is the number of node points in the FEM mesh, and M is the number of pixels for the representation of the conductivity. The second and third column show the numbers of node points and elements for the meshes that were used for the computation of the simulated EIT measurement data. Columns 3-5 show the number of nodes, elements and pixels for the reference reconstructions (conventional isotropic reconstruction) in the correct geometry Ω.

Measurement domain Ω	simulation of data		reconstruction		
	N_n	N_e	N_n	N_e	M
Ellipse (Case 1)	3052	5718	2741	5096	1048
Truncated ellipse (Case 2)	2963	5540	2680	4974	938
Fourier domain (Case 3)	3025	5588	2679	4972	1005
Chest CT (Case 4)	5116	9846	2740	5094	1060

5. **Numerical results.** We computed conventional isotropic reconstructions both in the correct domain Ω and in the incorrect model domain Ω_m. These reference reconstructions were obtained by minimizing

$$H(\gamma) = \|V - U(\gamma)\|^2 + W_\gamma(\gamma), \quad \gamma > 0, \tag{47}$$

where the unknown parameter vector $\gamma \in \mathbb{R}^M$ is the representation of isotropic conductivity in piecewise constant pixel basis and the regularization functional W_γ is as in equation (26). The solution of (47) was computed by transformation to

an unconstrained optimization problem by use of logarithmic parameterization $\varphi = \log(\gamma)$ and then finding the minimizer of

$$H(\varphi) = \|V - U(\exp(\varphi))\|^2 + W_\gamma(\exp(\varphi)) \tag{48}$$

with respect to φ using the Gauss-Newton method.

The discretization details of the true measurement domain Ω in each of the test cases for the minimization of (48) are given in Table 1. The mesh and pixel grid that were used for minimization of (48) in the incorrect model domain Ω_m were the same that were used for the minimization of (30) in the proposed method (with $N_n = 2677$, $N_e = 4968$ and $M = 1021$).

The regularization parameters for the penalty functionals (26)-(28) in minimization of (30) were tuned manually in the first test case for visually best image quality and then these values were fixed for the remaining test cases. The values were $\alpha_0 = 10^{-5}$, $\alpha_1 = 10$, $\beta_0 = 10^{-5}$ and $\beta_1 = 0.5$. In numerical tests, regularization in the scalar parameter was not needed and we used the parameter $\beta_2 = 0$. In each case, the Gauss-Newton optimization was started from the initial values $\eta = 1 \in \mathbb{R}^M$, $\theta = 0 \in \mathbb{R}^M$ and $\lambda = 1$ corresponding to isotropic unit conductivity. The regularization parameters for the functional W_γ in the minimization of (48) were chosen similarly considering the first test case in the correct domain Ω. The values were $\alpha_0 = 10^{-5}$ and $\alpha_1 = 10$.

The results for the Case 1 are shown in Figure 3, top row of Figure 7 and top left in Figure 8. The target conductivity and true measurement domain Ω is shown in the top left in Figure 3. The reconstruction in the top right is the conventional reconstruction of isotropic conductivity using the correct domain Ω. The reconstruction was obtained by minimization of (48). The bottom left is the isotropic reconstruction by minimization of (48) using the incorrect model domain Ω_m. The bottom right shows the reconstruction with the proposed method using the incorrect model domain Ω_m. The image shows the determinant $\eta = (\det \gamma_e)^{1/2}$ of the uniformly anisotropic conductivity γ_e in the isothermal coordinates $F_i(x)$, i.e., the displayed quantity is $\eta(\mathrm{Re}(F_i(x)), \mathrm{Im}(F_i(x)))$. The uniformly anisotropic conductivity $\gamma_e := \hat{\gamma}_{\lambda,\theta,\eta}$ (see 8) was computed by minimization of (30) using the model domain Ω_m. The top row of Figure 7 shows the reconstructed parameters η and θ in the model domain Ω_m. Using the reconstructed conductivity γ_e, the numerical approximation of the map $x \mapsto F_i(x)$ was obtained by solving equations (14)-(17) as explained in Section 4.2. The images in Figure 8 show for each of the four test cases the recovered isothermal coordinates $F_i(x_k)$ corresponding to set of points $\{x_k\}$ that define uniform grid in the model domain Ω_m. The solid line in the subfigures in Figure 8 show the boundary $\partial\Omega$ of the measurement domain.

The corresponding results for Case 2 are shown in Figure 4, the second row of Figure 7 and top right in Figure 8. For Case 3 the results are shown in Figure 5, the third row of Figure 7 and bottom left in Figure 8, and for Case 4 the results are shown in Figure 6, the bottom row of Figure 7 and bottom right in Figure 8.

6. **Discussion.** As can be seen from Figures 3-6, the conventional reconstruction of isotropic conductivity using the incorrect model domain Ω_m has severe reconstruction errors in all cases. The effect of incorrectly modeled geometry are seen as spurious details, especially near the boundary of the model domain. On the other hand, when using the same incorrect model geometry Ω_m, the proposed method produces reconstructions that are nearly similar to the conventional reconstruction that is computed in the correct geometry Ω, and also the shape of the domain has

been recovered reasonably well in all test cases. These findings indicate that the proposed approach can efficiently eliminate reconstruction errors that arise from inaccurately known measurement domain in EIT in the two-dimensional case.

To explain the good performance of our shape-deforming reconstruction method, let us consider properties of the conformal map G. Assume that a modeling map $f_m : \partial\Omega \to \partial\Omega_m$ of the boundary, which is a $C^{1,\alpha}$-smooth diffeomorphism, is a boundary value of $C^{1,\alpha}$-smooth diffeomorphisms $F_m^{in} : \Omega \to \Omega_m$ and $F_m^{out} : \mathbb{R}^2 \setminus \overline{\Omega} \to \mathbb{R}^2 \setminus \overline{\Omega}_m$, that is, $F_m^{in}|_{\partial\Omega} = f_m$ and $F_m^{out}|_{\partial\Omega} = f_m$ (for the existence of such maps, see [43]). These maps can be considered as the modeling maps of the interior domain and the exterior domain. Together they define the map $F_m : \mathbb{R}^2 \to \mathbb{R}^2$,

$$F_m(x) = \begin{cases} F_m^{in}(x), & x \in \Omega, \\ f_m(x), & x \in \partial\Omega, \\ F_m^{out}(x), & x \in \mathbb{R}^2 \setminus \overline{\Omega}. \end{cases}$$

Let us assume that

$$\begin{aligned} &\|DF_m^{in}(x) - I\|_{L(\mathbb{R}^2,\mathbb{R}^2)} \le \varepsilon_0, \quad x \in \Omega, \\ &\|DF_m^{out}(x) - I\|_{L(\mathbb{R}^2,\mathbb{R}^2)} \le \varepsilon_0, \quad x \in \mathbb{R}^2 \setminus \overline{\Omega}, \end{aligned} \tag{49}$$

where $0 < \varepsilon_0 < 1$, DF_m^{in} is the Jacobian matrix of map F_m^{in} and $I \in \mathbb{R}^{2\times 2}$ is the identity matrix. Then $F_m : \mathbb{R}^2 \to \mathbb{R}^2$ is a K_0-quasiconformal map, where

$$K_0 = \frac{1+\varepsilon_0}{1-\varepsilon_0}. \tag{50}$$

Let now $F_e^{in} : \Omega \to \Omega_m$ be a Teichmüller extremal map (quasiconformal with smallest possible dilation) with boundary value $F_e^{in}|_{\partial\Omega} = f_m$. Also, let $F_{mod}^{out} : \mathbb{R}^2 \setminus \overline{\Omega} \to \mathbb{R}^2 \setminus \overline{\Omega}_m$ be a quasiconformal map having boundary value $F_{mod}^{out}|_{\partial\Omega} = f_m$, whose dilatation is smaller or equal to the dilatation of the exterior map F_m^{out}.

Denote the Riemann sphere by $\mathbb{S}^2 = \mathbb{R}^2 \cup \{\infty\}$. Now F_{mod}^{out} can be extended to a map $\mathbb{S}^2 \setminus \overline{\Omega} \to \mathbb{S}^2 \setminus \overline{\Omega}_m$ with infinity as a fixed point. It is not clear if, among the quasiconformal maps $H : \mathbb{S}^2 \setminus \overline{\Omega} \to \mathbb{S}^2 \setminus \overline{\Omega}_m$ with infinity as a fixed point and the prescribed boundary values, there exist one whose dilatation is the smallest.

Let K^{in} and K be the dilatations of F_e^{in} and F_{mod}^{out}, correspondingly. Then

$$K^{in} \le K_0 \quad \text{and} \quad K \le K_0. \tag{51}$$

Let us define ε_1 such that $K = (1+\varepsilon_1)/(1-\varepsilon_1)$. Then $0 \le \varepsilon_1 \le \varepsilon_0$. Define

$$F_{mod}^{plane}(x) = \begin{cases} F_e^{in}(x), & x \in \Omega, \\ f_m(x), & x \in \partial\Omega, \\ F_{mod}^{out}(x), & x \in \mathbb{R}^2 \setminus \overline{\Omega}. \end{cases}$$

Then $F_{mod}^{plane} : \mathbb{R}^2 \to \mathbb{R}^2$ quasiconformal. Let us now consider the map $g : \mathbb{R}^2 \to \mathbb{R}^2$ defined by $g = F_i \circ F_{mod}^{plane}$. As the restriction $g|_\Omega : \Omega \to \Omega_i$ is conformal, we see that $g : \mathbb{R}^2 \to \mathbb{R}^2$ map is K-quasiconformal. Moreover, it satisfies $g|_\Omega = G$. As $g : \mathbb{R}^2 \to \mathbb{R}^2$ is K-quasiconformal satisfies by [3, Cor. 3.10.4 and p. 81] a quasisymmetry estimate

$$\frac{|g(x)-g(z)|}{|g(y)-g(z)|} \le \eta_K\left(\frac{|x-z|}{|y-z|}\right), \qquad \frac{|x-z|}{|y-z|} \le \eta_K\left(\frac{|g(x)-g(z)|}{|g(y)-g(z)|}\right), \tag{52}$$

for all $x, y, z \in \mathbb{R}^2$, where $\eta_K(t) = \lambda(K)^{2K} \max(t^K, t^{1/K})$ for $t \ge 0$ and

$$1 \le \lambda(K) \le \frac{1}{16} e^{\pi K}, \quad \lim_{K\to 1} \lambda(K) = 1.$$

Let us now consider the meaning of the estimate (52). We started from the assumption that the boundary modeling map f_m is the boundary value of diffeomorphisms satisfying estimates (50) and (51). Then F_{mod}^{out} is a quasiconformal map having boundary value f_m with the dilatation K. This dilatation satisfies $K \leq K_0$ and it may be much closer to one than K_0. For instance, if f_m happens by chance to be a boundary value of a conformal map from the exterior of Ω to the exterior of Ω_m, the dilatation K has the value one, and $\varepsilon_1 = 0$. Using this map we obtained the K-quasiconformal homeomorphism $g : \mathbb{R}^2 \to \mathbb{R}^2$ and the image $\Omega_i = g(\Omega)$. If $K - 1$ is very small, the map g satisfies a global estimate (52) where $\eta_K(t)$ is quite close to the identity map. The closer K is to 1, the closer $\eta_K(t)$ is to identity. Next, let us assume for simplicity that $0 < \varepsilon_0 < 10^{-2}$, so that $K - 1 \leq 3\varepsilon_1$, and that $\operatorname{diam}(\Omega) \leq 1$. Then, if $x, y, z \in \partial\Omega$ are arbitrary points which mutual distances are larger than $h = \varepsilon_0$, we see from (52) that the relative distances of the points $x, y, z \in \partial\Omega$ and the points $x' = g(x), y' = g(y), z' = g(z) \in \partial\Omega_i$ satisfy

$$\begin{aligned} (53) \qquad & \left| \frac{|x'-z'|}{|y'-z'|} - \frac{|x-z|}{|y-z|} \right| \leq \lambda(K)^{2K} h^{1/K} \frac{1}{K^2 |\ln h|} (K-1) + (\lambda(K)^{2K} - 1) \\ & \leq L^{2(1+3\varepsilon_1)} \frac{6\varepsilon_1}{|\ln \varepsilon_0|} + (L^{2(1+3\varepsilon_1)} - 1), \quad L = \lambda(1 + 3\varepsilon_1). \end{aligned}$$

Note that the last term is of the form $O(\varepsilon_1/|\log(\varepsilon_0)|) \leq O(\varepsilon_1/|\log(\varepsilon_1)|)$ as $\varepsilon_1 \leq \varepsilon_0$ and $\varepsilon_1 \to 0$. Thus, is the scales larger that $h = \varepsilon_0$ the boundaries $\partial\Omega$ and $\partial\Omega_i$ are, up to small errors, equivalent in an Euclidean similarity transform. We emphasize that in the construction ε_1 may be much smaller than ε_0. In this case the errors in (53) are much smaller than in the worst case where ε_1 in equal to ε_0. This may explain why the reconstruction of the domain in our practical examples are so good.

Theoretically, the reconstruction may also fail: If one by chance has a boundary modeling map f_m which is a boundary value of a conformal map $F_m^{in} : \Omega \to \Omega_m$, then the map F_i is just the identical map and the reconstructed image of the domain Ω_i is equal to the original model domain Ω_m. Due to the Riemann mapping theorem, Ω_m can be an arbitrary bounded simply connected domain.

Summarizing: If the boundary modeling map happens to be close to the set

$$\begin{aligned} X = \{h|_{\partial\Omega} \quad ; \quad & h : \mathbb{R}^2 \setminus \overline{\Omega} \to \mathbb{R}^2 \setminus \overline{\Omega}_m \text{ is conformal}, \\ & h : \mathbb{R}^2 \setminus \Omega \to \mathbb{R}^2 \setminus \Omega_m \text{ is homeomorphism}\} \end{aligned}$$

then Ω_i is close to Ω up to a similarity transformation.

In this study, we considered the EIT problem with unknown boundary in the 2D case. In the clinical applications, such as imaging of the lung function, the measurements are taken at the surface of a three-dimensional (3D) body and the situation becomes more complicated. The present 2D formulation would in 3D be valid to a case where the conductivity, boundary and electrodes are translationally invariant in the direction perpendicular to the 2D plane and the domain is truncated from the top and bottom with Neumann zero conditions. Such assumptions are not very realistic when imaging the human body and the question that how good approximations the approach would produce for the 2D cross section of the 3D conductivity in a case of measurements from a 3D target that is not translationally symmetric is yet open. Answering this question is left for future studies.

Another practical complictation with the method is that the solution of (4.6) involves selection of 5 regularization parameters. We are not aware of any systematic algorithms for choosing such many regularization parameters. In the present

manuscript, we tuned the parameters manually in the first test case and used the same parameters in all of the remaining test cases, and found that the method worked robustly with the fixed parameter values. Therefore we believe that for a given measurement setup and target type the algorithm could be made to work by tuning the parameters only once and then using fixed values.

REFERENCES

[1] A. Adler, R. Guardo and Y. Berthiaume, *Impedance imaging of lung ventilation: Do we need to account for chest expansion?*, IEEE Trans. Biomed. Eng., **43** (1996), 414–420.

[2] L. Ahlfors, "Lectures on Quasiconformal Mappings," Van Nostrand Mathematical Studies, No. 10, D. Van Nostrand Co., Inc., Toronto, Ont.-New York-London, 1966.

[3] K. Astala, T. Iwaniec and G. Martin, "Elliptic Partial Differential Equations and Quasiconformal Mappings in the Plane," Princeton Mathematical Series, **48**, Princeton University Press, Princeton, NJ, 2009.

[4] K. Astala, M. Lassas and L. Päivärinta, *Calderón's inverse problem for anisotropic conductivity in the plane*, Comm. Partial Differential Equations, **30** (2005), 207–224.

[5] K. Astala and L. Päivärinta, *Calderón's inverse conductivity problem in the plane*, Ann. of Math. (2), **163** (2006), 265–299.

[6] K. Astala, J. L. Mueller, L. Paivarinta and S. Siltanen, *Numerical computation of complex geometrical optics solutions to the conductivity equation*, Applied and Computational Harmonic Analysis, **29** (2010), 2–17.

[7] D. C. Barber and B. H. Brown, *Applied potential tomography*, J. Phys. E: Sci. Instrum., **17** (1984), 723–733.

[8] A. Boyle, W. R. B. Lionheart, C. Gómez-Laberge and A. Adler, *Evaluating deformation corrections in electrical impedance tomography*, in "Proc. of the 2008 Electrical Impedance Tomography Conference," Dartmouth College, Hanover, New Hampshire, USA, June 16–18, (2008). Available from: `http://engineering.dartmouth.edu/eit2008/EIT_Conference_2008.pdf`.

[9] A. Boyle and A. Adler, *The impact of electrode area, contact impedance and boundary shape on EIT images*, Physiological Measurement, **32** (2011), 745–754

[10] V. Bozin, N. Lakic, V. Markovic and M. Mateljevic, *Unique extremality*, J. Anal. Math. **75** (1998), 299–338.

[11] R. Brown and G. Uhlmann, *Uniqueness in the inverse conductivity problem for non-smooth conductivities in two dimensions*, Comm. Partial Differential Equations, **22** (1997), 1009–1027.

[12] A. Calderón, *On an inverse boundary value problem*, Seminar on Numerical Analysis and its Applications to Continuum Physics (Rio de Janeiro, 1980), Soc. Brasil Mat., Rio de Janeiro, (1980), 65–73.

[13] M. Cheney, D. Isaacson and J. C. Newell, *Electrical impedance tomography*, SIAM Review, **41** (1999), 85–101.

[14] K.-S.Cheng, D. Isaacson, J. C. Newell and D. G. Gisser, *Electrode models for electric current computed tomography*, IEEE Trans. Biomed. Eng., **36** (1989), 918–924.

[15] E. L. V. Costa, C. N. Chaves, S. Gomes, M. A. Beraldo, M. S. Volpe, M. R. Tucci, I. A. L. Schettino, S. H. Bohm, C. R. R. Carvalho, H. Tanaka, R. G. Lima and M. B. A. Amato, *Real-time detection of pneumothorax using electrical impedance tomography*, Crit. Care. Med., **36** (2008), 1230–1238.

[16] T. Dai, C. Gomez-Laberge and A. Adler, *Reconstruction of conductivity changes and electrode movements based on EIT temporal sequences*, Physiol. Meas., **29** (2008), S77–S88.

[17] E. Gersing, B. Hoffman and M. Osypka, *Influence of changing peripheral geometry on electrical impedance tomography measurements*, Medical & Biological Engineering & Computing, **34** (1996), 359–361.

[18] A. Greenleaf, Y. Kurylev, M. Lassas, and G. Uhlmann, *Full-wave invisibility of active devices at all frequencies*, Comm. Math. Phys., **275** (2007), 749–789.

[19] A. Greenleaf, Y. Kurylev, M. Lassas and G. Uhlmann, *Invisibility and inverse problems*, Bull. Amer. Math. Soc. (N.S.), **46** (2009), 55–97.

[20] A. Greenleaf, Y. Kurylev, M. Lassas and G. Uhlmann, *Cloaking devices, electromagnetic wormholes and transformation optics*, SIAM Review, **51** (2009), 3–33.

[21] A. Greenleaf, M. Lassas and G. Uhlmann, *On nonuniqueness for Calderón's inverse problem*, Math. Res. Lett., **10** (2003), 685–693.
[22] A. Greenleaf, M. Lassas and G. Uhlmann, *Anisotropic conductivities that cannot detected in EIT*, Physiological Measurement, **24** (2003), 413–420.
[23] G. Hahn, A. Just, T. Dudykevych, I. Frerichs, J. Hinz, M. Quintel and G. Hellige, *Imaging pathologic pulmonary air and fluid accumulation by functional and absolute EIT*, Physiol. Meas., **27** (2006), S187–S198.
[24] D. Isaacson, J. Mueller, J. C. Newell and S. Siltanen, *Reconstructions of chest phantoms by the d-bar method for electrical impedance tomography*, IEEE Trans. Med. Im., **23** (2004), 821–828.
[25] D. Isaacson, J. L. Mueller, J. C. Newell and S. Siltanen, *Imaging cardiac activity by the D-bar method for electrical impedance tomography*, Physiological Measurement, **27** (2006), S43–S50.
[26] H. Jain, D. Isaacson, P. M. Edic and J. C. Newell, *Electrical impedance tomography of complex conductivity distributions with noncircular boundary*, IEEE Trans. Biomed. Eng., **44** (1997), 1051–1060.
[27] J. P. Kaipio, V. Kolehmainen, E. Somersalo and M. Vauhkonen, *Statistical inversion and Monte Carlo sampling methods in electrical impedance tomography*, Inverse Problems, **16** (2000), 1487–1522.
[28] R. Kohn and M. Vogelius, *Identification of an unknown conductivity by means of measurements at the boundary*, in "Inverse Problems" (New York, 1983), SIAM-AMS Proc., **14**, AMS, Providence, RI, (1984), 113–123.
[29] R. Kohn, H. Shen, M. Vogelius and M. Weinstein, *Cloaking via change of variables in electrical impedance tomography*, Inverse Problems, **24** (2008), 015016, 21 pp.
[30] K. Knudsen, M. Lassas, J. L. Mueller and S. Siltanen, *Regularized D-bar method for the inverse conductivity problem*, Inverse Problems and Imaging, **3** (2009), 599–624.
[31] V. Kolehmainen, M. Vauhkonen, P. A. Karjalainen and J. P. Kaipio, *Assessment of errors in static electrical impedance tomography with adjacent and trigonometric current patterns*, Physiological Measurement, **18** (1997), 289–303.
[32] V. Kolehmainen, M. Lassas and P. Ola, *The inverse conductivity problem with an imperfectly known boundary*, SIAM J. Appl. Math., **66** (2005), 365–383.
[33] V. Kolehmainen, M. Lassas and P. Ola, *The inverse conductivity problem with an imperfectly known boundary in three dimensions*, SIAM J. Appl. Math., **67** (2007), 1440–1452.
[34] V. Kolehmainen, M. Lassas and P. Ola, *Calderón's inverse problem with an imperfectly known boundary and reconstruction up to a conformal deformation*, SIAM J. Math. Anal., **42** (2010), 1371–1381.
[35] V. Kolehmainen, M. Lassas and P. Ola, *Electrical impedance tomography problem with inaccurately known boundary and contact impedances*, IEEE Trans. Med. Im., **27** (2008), 1404–1414.
[36] M. Lassas and G. Uhlmann, *On determining Riemannian manifold from the Dirichlet-to-Neumann map*, Annales Scientifiques de l'Ecole Normale Superieure (4), **34** (2001), 771–787.
[37] W. Lionheart, *Conformal uniqueness results in anisotropic electrical impedance imaging*, Inverse Problems, **13** (1997), 125–134.
[38] W. Lionheart, *Boundary shape and electrical impedance tomography*, Inverse Problems, **14** (1998), 139–147.
[39] A. Nachman, *Global uniqueness for a two-dimensional inverse boundary value problem*, Ann. Math. (2), **143** (1996), 71–96.
[40] A. Nissinen, V. Kolehmainen and J. P. Kaipio, *Compensation of modelling errors due to unknown domain boundary in electrical impedance tomography*, IEEE Trans. Med. Imag., **30** (2011), 231–242.
[41] A. Nissinen, V. Kolehmainen and J. P. Kaipio, *Reconstruction of domain boundary and conductivity in electrical impedance tomography using the approximation error approach*, International Journal for Uncertainty Quantification, **1** (2011), 203–222.
[42] J. Nocedal and S. J. Wright, "Numerical Optimization," Second edition, Springer Series in Operations Research and Financial Engineering, Springer, New York, 2006.
[43] Ch. Pommerenke, "Boundary Behaviour of Conformal Maps," Grundlehren der Mathematischen Wissenschaften [Fundamental Principles of Mathematical Sciences], **299**, Springer-Verlag, Berlin, 1992.
[44] S. Siltanen, J. Mueller and D. Isaacson, *An implementation of the reconstruction algorithm of A. Nachman for the 2D inverse conductivity problem,* Inverse Problems, **16** (2000), 681–699. Erratum: Inverse Problems, **17**, 1561–1563.

[45] M. Soleimaini, C. Gómez-Laberge and A. Adler, *Imaging of conductivity changes and electrode movement in EIT*, Physiol. Meas., **27** (2006), S103–S113.
[46] E. Somersalo, M. Cheney and D. Isaacson, *Existence and uniqueness for electrode models for electric current computed tomography*, SIAM J. Appl. Math., **52** (1992), 1023–1040.
[47] K. Strebel, *On the existence of extremal Teichmüller mappings*, J. Anal. Math., **30** (1976), 464–480.
[48] J. Sylvester, *An anisotropic inverse boundary value problem*, Comm. Pure Appl. Math., **43** (1990), 201–232.

Received November 2011; revised May 2012.

E-mail address: ville.kolehmainen@uef.fi
E-mail address: matti.lassas@helsinki.fi
E-mail address: petri.ola@helsinki.fi
E-mail address: samuli.siltanen@helsinki.fi

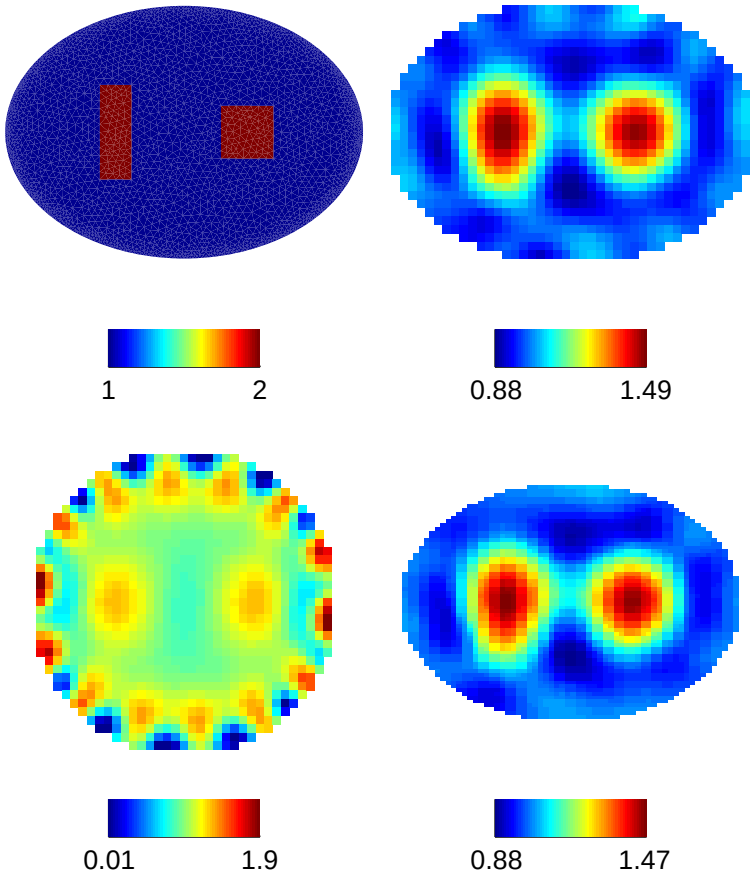

Figure 3. (Case 1). Top left: True conductivity and the measurement domain Ω. Top right: Reconstruction of isotropic conductivity using the correct domain Ω. Bottom left: Reconstruction of isotropic conductivity using incorrect model geometry Ω_m. Bottom right: Reconstruction with the proposed method using the incorrect model geometry Ω_m. The image shows the parameter η in the isothermal coordinates $x \mapsto F_i(x)$ (i.e., displayed quantity is $\eta(\mathrm{Re}(F_i(x)), \mathrm{Im}(F_i(x)))$).

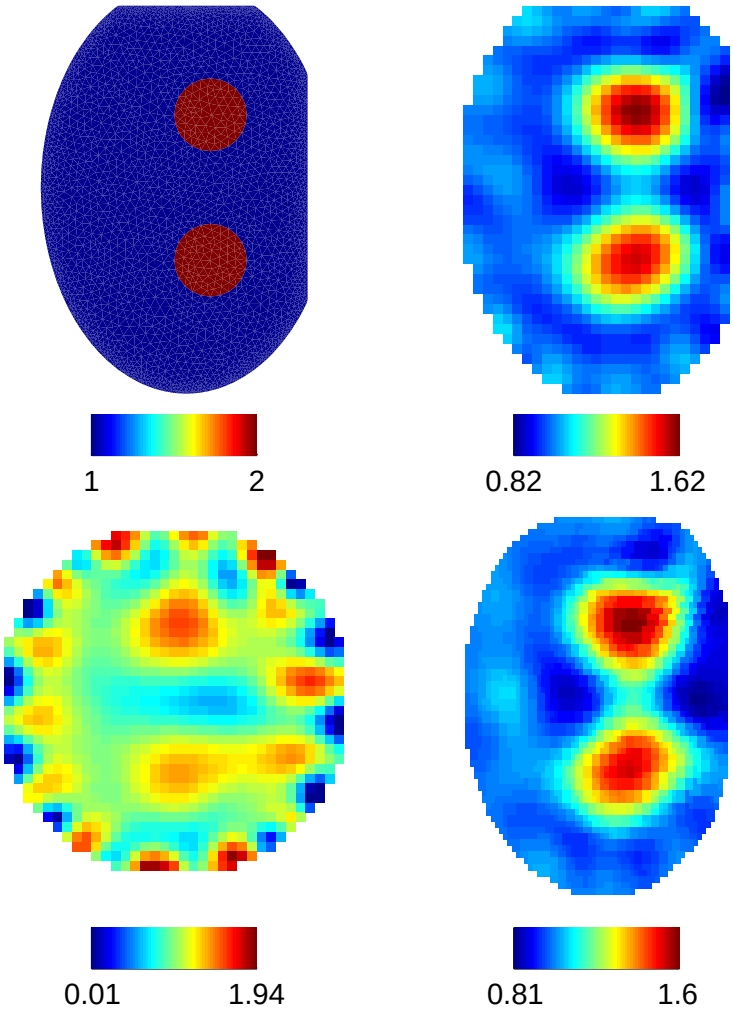

Figure 4. (Case 2). Top left: True conductivity and the measurement domain Ω. Top right: Reconstruction of isotropic conductivity using the correct domain Ω. Bottom left: Reconstruction of isotropic conductivity using incorrect model geometry Ω_m. Bottom right: Reconstruction with the proposed method using the incorrect model geometry Ω_m. The image shows the parameter η in the isothermal coordinates $x \mapsto F_i(x)$ (i.e., displayed quantity is $\eta(\mathrm{Re}(F_i(x)), \mathrm{Im}(F_i(x))))$

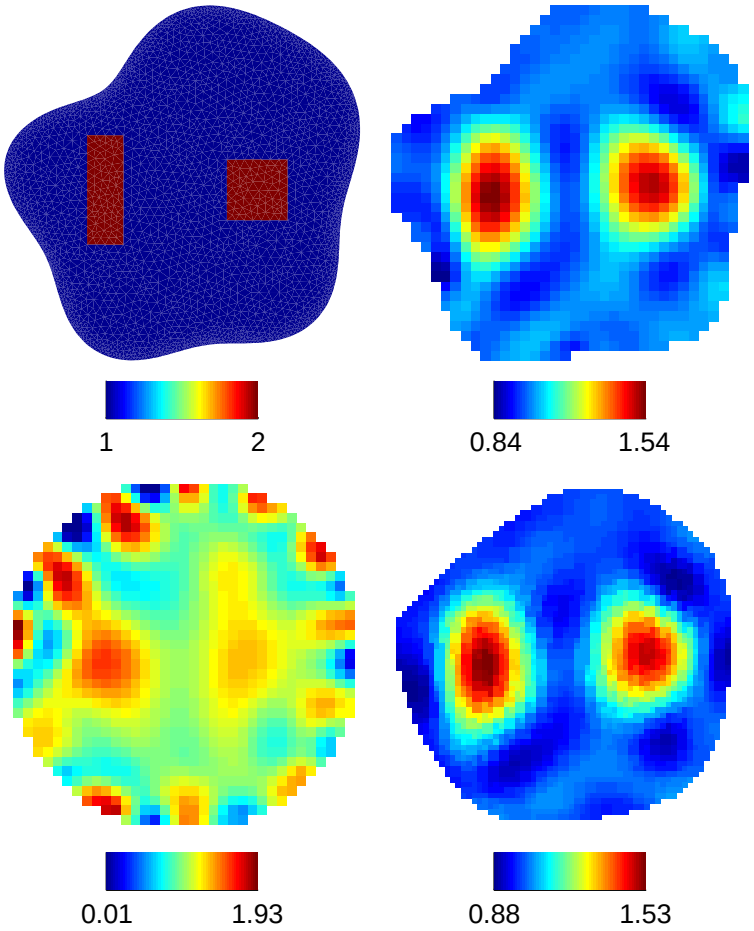

Figure 5. (Case 3). Top left: True conductivity and the measurement domain Ω. Top right: Reconstruction of isotropic conductivity using the correct domain Ω. Bottom left: Reconstruction of isotropic conductivity using incorrect model geometry Ω_m. Bottom right: Reconstruction with the proposed method using the incorrect model geometry Ω_m. The image shows the parameter η in the isothermal coordinates $x \mapsto F_i(x)$ (i.e., displayed quantity is $\eta(\mathrm{Re}(F_i(x)), \mathrm{Im}(F_i(x))))$

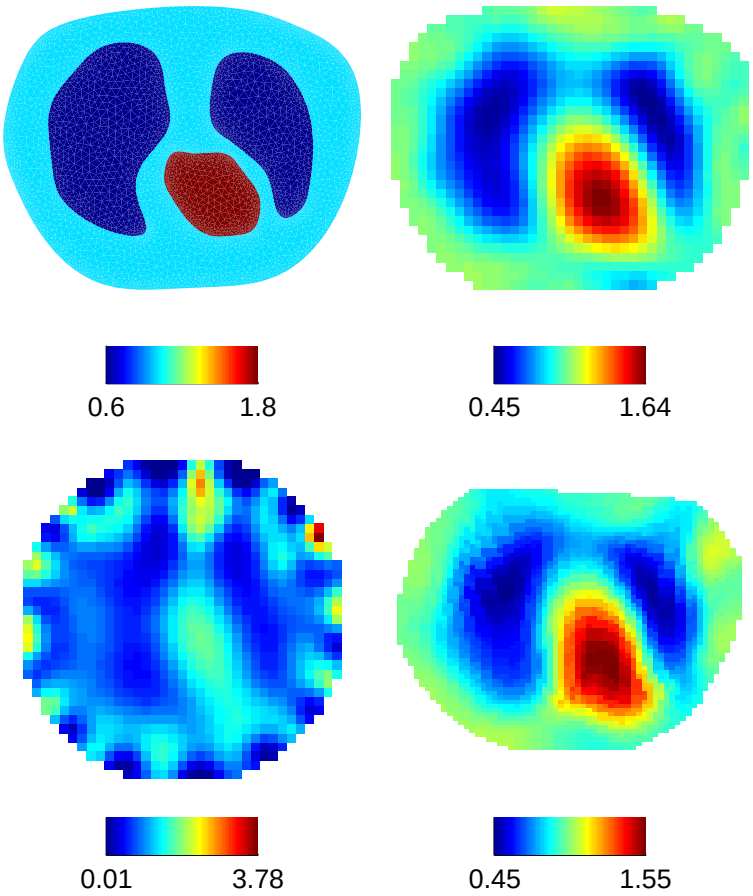

Figure 6. (Case 4). Top left: True conductivity and the measurement domain Ω. The domain Ω is a cross section of human chest obtained from a CT reconstruction. Top right: Reconstruction of isotropic conductivity using the correct domain Ω. Bottom left: Reconstruction of isotropic conductivity using incorrect model geometry Ω_m. Bottom right: Reconstruction with the proposed method using the incorrect model geometry Ω_m. The image shows the parameter η in the isothermal coordinates $x \mapsto F_i(x)$ (i.e., displayed quantity is $\eta(\mathrm{Re}(F_i(x)), \mathrm{Im}(F_i(x)))$)

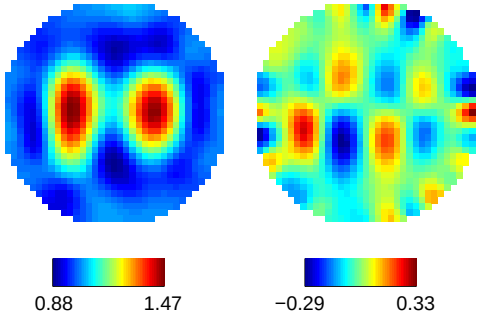

(Case 1)

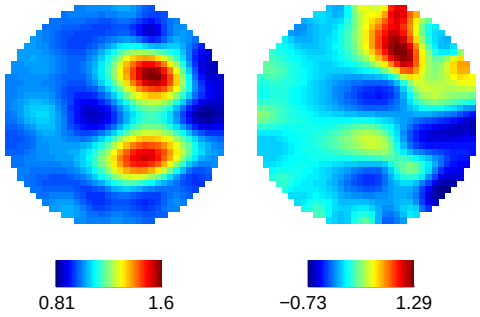

(Case 2)

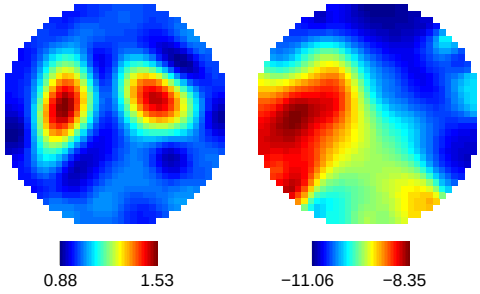

(Case 3)

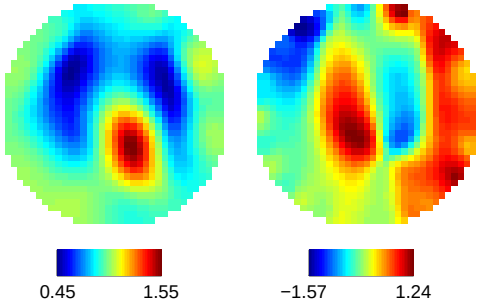

(Case 4)

FIGURE 7. Results of step 1 of the algorithm for the test cases 1-4. Left: η. Right: θ. The estimates were obtained by minization of (30) using the model domain Ω_m (circle with radius of 14cm).

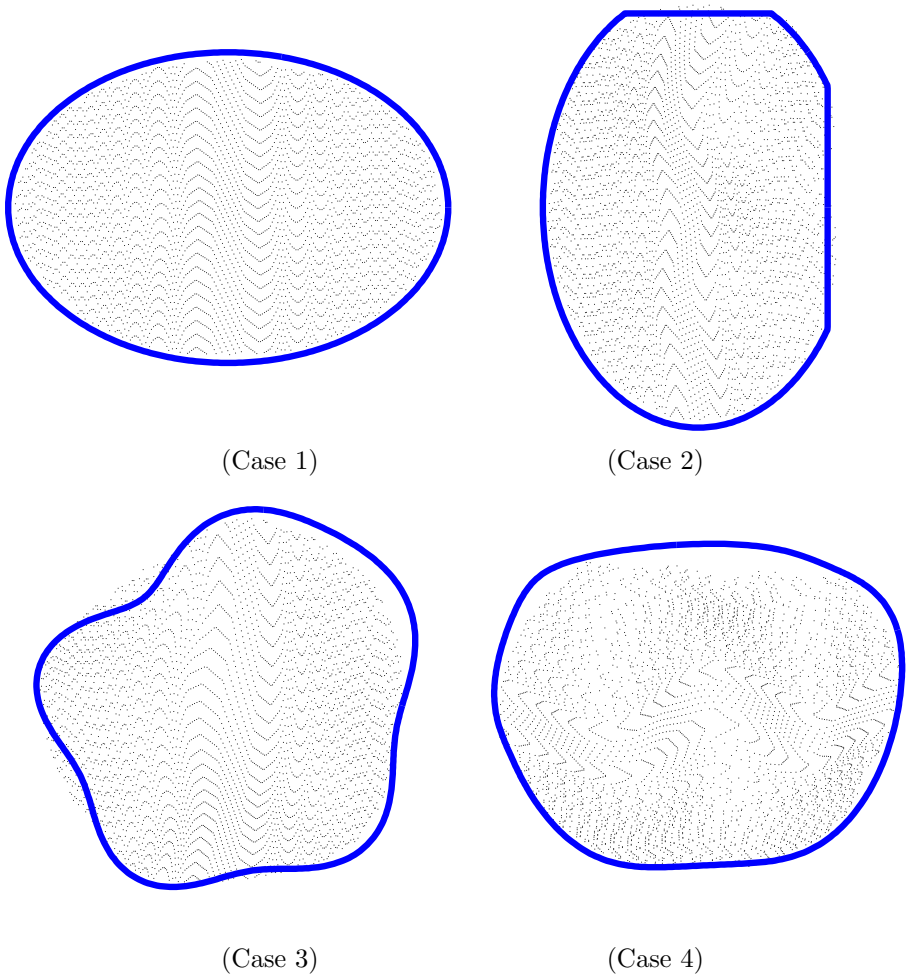

Figure 8. Approximate recovery of the deformation and domain boundary. Each subfigure shows the isothermal coordinates $z \mapsto F_i(x)$ that were obtained from the numerical solution of (14)-(17). The boundary $\partial\Omega$ of the true measurement domain is shown with solid line.